Surface Cyclolysis in the North Pacific Ocean. Part I: A Synoptic Climatology

JONATHAN E. MARTIN, RHETT D. GRAUMAN, AND NATHAN MARSILI

Department of Atmospheric and Oceanic Sciences, University of Wisconsin—Madison, Madison, Wisconsin

(Manuscript received 20 January 2000, in final form 16 August 2000)

ABSTRACT

A continuous 11-yr sample of extratropical cyclones in the North Pacific Ocean is used to construct a synoptic climatology of surface cyclolysis in the region. The analysis concentrates on the small population of all decaying cyclones that experience at least one 12-h period in which the sea level pressure increases by 9 hPa or more. Such periods are defined as threshold filling periods (TFPs). A subset of TFPs, referred to as rapid cyclolysis periods (RCPs), characterized by sea level pressure increases of at least 12 hPa in 12 h, is also considered.

The geographical distribution, spectrum of decay rates, and the interannual variability in the number of TFP and RCP cyclones are presented. The Gulf of Alaska and Pacific Northwest are found to be primary regions for moderate to rapid cyclolysis with a secondary frequency maximum in the Bering Sea. Moderate to rapid cyclolysis is found to be predominantly a cold season phenomena most likely to occur in a cyclone with an initially low sea level pressure minimum. The number of TFP–RCP cyclones in the North Pacific basin in a given year is fairly well correlated with the phase of the El Niño–Southern Oscillation (ENSO) as measured by the multivariate ENSO index.

An analysis of the composite structure and evolution of cyclones containing a single RCP reveals that, on average, such storms undergo a significant period of cyclogenesis immediately prior to the commencement of decay. This cyclogenesis is characterized by the development of a sharply curved and progressively more negatively tilted upper-level shortwave trough. The sudden deamplification of this feature, which results in an abrupt reduction in the mid- and upper-tropospheric mass divergence above the surface cyclone, is the underlying physical factor responsible for the concurrent rapid cyclolysis at the surface. A complementary overview of this evolution from a potential vorticity (PV) perspective demonstrates that rapid cyclolysis at the surface is coincident with a weakening of the upper and lower PV anomalies and the acquisition of a downshear phase tilt to the anomalies. Thus, it is suggested that rapid cyclolysis events, though influenced by friction in the boundary layer, are initiated and largely controlled by synoptic-scale dynamical processes.

1. Introduction

The midlatitude cyclone has been the topic of considerable scientific inquiry since Bjerknes and Solberg (1922) first placed the instantaneous structure of the cyclone into the context of its evolution through an identifiable life cycle. In the conceptual model they introduced, known as the ''Norwegian'' model, the cyclone develops as a result of a perturbation on a pre-existing frontal boundary, the polar front, which separates tropical from polar air. As the cyclone develops, the polar front is gradually distorted by the circulation of the cyclone to create a warm front and cold front separated by a region of homogeneous warm air known as the warm sector. With continued progression through the life cycle, the cold front overtakes the warm front forming the occluded front and pinching the cyclone center off from the warm sector. As the cyclone decays, the area of precipitation diminishes, and the intersection of the original warm and cold frontal boundaries (known as the triple point) is found well to the south and east of the center of the decaying surface cyclone.

In the more than three-quarters of a century since this model was introduced, a number of significant advances in understanding have altered the way the cyclone life cycle is viewed. It is recognized today that cyclones do not generally develop as instabilities along a tropospheric deep, pre-existing frontal boundary, but occur as a result of a basic instability of the baroclinic westerly flow to a class of perturbations. A majority of the research undertaken with regard to the structure and dynamics of observed extratropical cyclones has focused on the incipient, developing, mature, and occluded stages of these systems (e.g., Palmen 1951; Penner 1955; Kreitzberg 1968; Reed 1979; Shapiro and Keyser 1990; Schultz and Mass 1993; Hobbs et al. 1996; Martin 1998, 1999). The dynamical and structural transformations associated with the decay stage of the extratropical cyclone (cyclolysis) have received almost no attention in prior research and are hardly mentioned in the Nor-

Corresponding author address: Prof. Jonathan E. Martin, Department of Atmospheric and Oceanic Sciences, University of Wisconsin—Madison, 1225 W. Dayton St., Madison, WI 53706.
E-mail: jon@meteor.wisc.edu

wegian model description of the life cycle. Equally unknown is the effect that cyclolysis has on the larger-scale environment within which it occurs. A more detailed understanding of the structural and dynamical processes associated with cyclolysis is therefore necessary in order to develop a comprehensive understanding of the complete extratropical cyclone life cycle. To date, studies of cyclolysis have been largely absent from the literature and, when considered at all, have been investigated most frequently from a statistical point of view. This series of papers aims to fortify and extend these initial studies by presenting both a continuous, long-term synoptic climatology of north Pacific cyclolysis (this paper) as well as a detailed synoptic diagnostic case study of a particularly robust example of cyclolysis (Part II).

In order to develop greater understanding of the climatology of cyclolysis, the present paper presents the results of a continuous 11-yr census of cyclone decay in the North Pacific Ocean along with an analysis of the composite structure and evolution of 180 particularly rapid cyclolysis events observed over that period. The primary objectives of this study are 1) to determine the geographical distribution of moderate to rapid surface cyclolysis in the North Pacific Ocean, 2) to characterize the spectrum of cyclolytic rates in that region, 3) to examine the interseasonal variability of moderate to rapid cyclolysis, and 4) to gain a basic understanding of the physical factors involved in observed cases of rapid cyclolysis. In order to accomplish these goals the paper will be organized as follows. In section 2 we present a review of prior work on the issue of cyclolysis. In section 3 we will describe the dataset and analysis method used in the construction of the synoptic climatology described here. Aspects of the frequency and geographic distribution of moderate to rapid cyclolysis events will be presented in section 4. That section also contains an analysis of the interannual variability of the frequency distributions suggesting a link between this variability and the large-scale climate perturbations associated with El Niño–Southern Oscillation (ENSO). An analysis of the composite structure and evolution of the rapid cyclolysis events is presented in section 5. Finally, our conclusions and suggestions for future research will be described in section 6.

2. Review of prior work on cyclolysis

In one of the earliest statistical studies that includes reference to cyclone decay, Zishka and Smith (1980) investigated the climatology of cyclones and anticyclones using a 2° latitude–longitude grid spanning North America and surrounding ocean environments for the months of January and July in the period 1950–77. In that study the total areal statistics, distributions of cyclone–anticyclone events, genesis, lysis, and relative preferred propagation tracks were determined. Cyclolysis during January most frequently occurred along the coast of northern Oregon, Washington, southern British Columbia, and southern Alaska (Fig. 1a). The intensity and frequency of July cyclones were much lower compared to the winter months, as were the number of cyclolytic events. The region of maximum decay in July was located farther north in central British Columbia and along the southern coast of Alaska (not shown).

In work that extended the climatology of explosive cyclones performed by Sanders and Gyakum (1980), Roebber (1984) examined the 1979–82 cold seasons and compared them to the previous 3-yr sample (1976–79). In addition, a climatology of formation, maximum deepening, and dissipation positions for all cyclones in a single year (1980–81) was compiled. It was found that the Gulf of Alaska (Fig. 1b) and an area between Newfoundland, Greenland, and Iceland (not shown) were preferential regions for cold season cyclolysis in the 1-yr sample.

Some insight into the life cycle of associated upper-level disturbances arose from the work of Sanders (1988), who tracked mobile troughs once a day at 0000 UTC in the Northern Hemisphere 500-hPa analysis during nine cold seasons, October 1976 through May 1984, and again during the 1985/86 cold season. These troughs were identified in the 552-dam geopotential height contour as it was suggested to represent the optimum location of the major band of the circumpolar westerlies. Mobile troughs along this contour were identified each day with dates and locations of their first and final appearances noted. There were several regions of apparent high frequency trough deaths in the nine cold seasons but only one region of maximum trough decay in the Pacific Ocean, centered at 50°N, 140°W (Fig. 1c). The high number of trough deaths associated with this maximum region encompassed the Gulf of Alaska, the northwestern United States, and the coastlines of British Columbia and southern Alaska. Sanders noted that regions of excess trough deaths might be related to orographic effects as they tended to lie roughly 1000 km upwind from major masses of elevated terrain. It was also noted that a preference for trough deaths was found to occur in southwesterly flow. Lefevre and Nielsen-Gammon (1995) generalized this work by developing an objective scheme for the identification and tracking of mobile troughs in the Northern Hemisphere. Their distribution of trough deaths was similar to Sanders (1988) and showed the Gulf of Alaska region to be an active graveyard for upper troughs throughout the year.

The life cycles of rapidly deepening, North Pacific, cold season (October through March) surface cyclones from 1975 through 1983 were investigated by Gyakum et al. (1989). Data were based upon the National Meteorological Center's (now the National Centers for Environmental Prediction) final Northern Hemisphere surface analysis, performed every six hours. All cyclones included in their statistics were required to have existed for at least 24 h and must have deepened at least 24 hPa in some 24-h period during the life cycle. Thus,

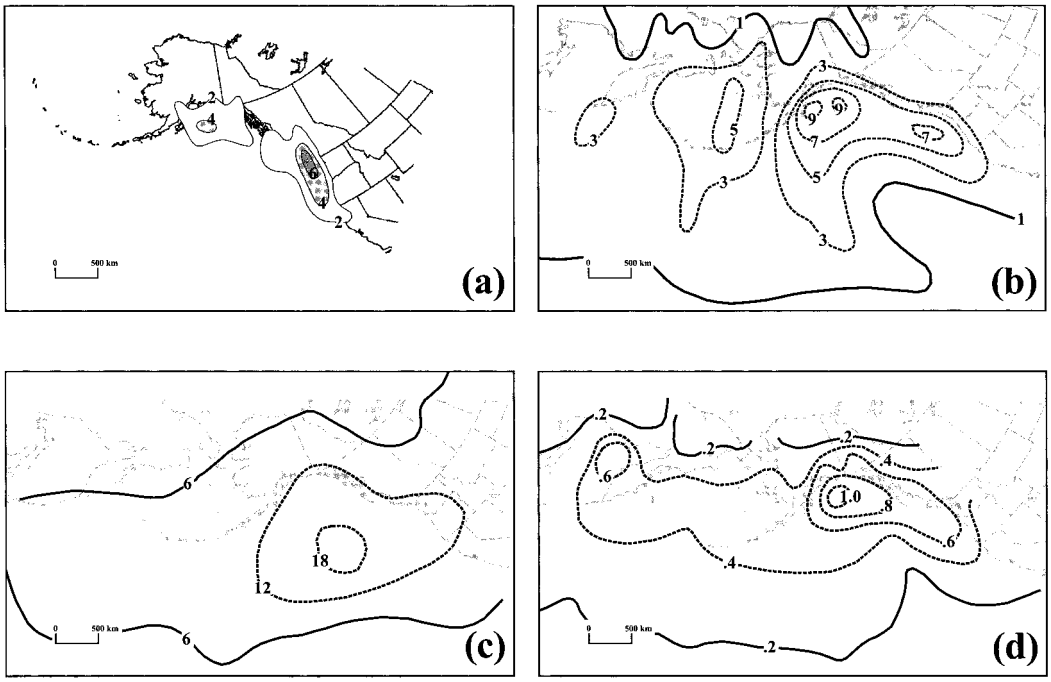

FIG. 1. (a) Areal distribution of Jan cyclolysis from 1950 to 1977. Values represent 28-yr total number of decaying cyclones. Adapted from Zishka and Smith (1980). (b) Cumulative distribution of cyclone dissipation positions during a 1-yr sample (1980–81). Adapted from Roebber (1984). (c) Geographic distributions of 500-hPa mobile trough deaths during nine cold seasons (Oct–May). Adapted from Sanders (1988). (d) Explosive cyclone dissipation position frequencies per 30 days in 5° × 5° quadrilaterals. Adapted from Gyakum et al. (1989).

each cyclone in their sample was a ''bomb'' (Sanders and Gyakum 1980). Certain life cycle characteristics of these storms were explored by showing the locations of formation, maximum deepening, and dissipation. Dissipation positions were defined as the location where a given cyclone could no longer be identified by a closed pressure contour (analyzed at 4-hPa intervals) in the sea level pressure field. The results showed that dissipation positions were confined exclusively to a region between 50° and 65°N with local maxima in the Gulf of Alaska, Bering Sea, and east of the Kamchatka Peninsula (Fig. 1d).

Bell and Bosart (1989) used 15 yr (1963–77) of Northern Hemisphere 500-hPa geopotential heights to construct a climatology of 500-hPa closed circulation centers. These centers, defined by at least one closed 30-m contour around a central minimum or maximum geopotential height value, were identified objectively from twice-daily National Meteorological Center analysis grids. Intensification and decay of cyclonic circulation centers were tracked for all seasons of the year. The Gulf of Alaska and the west coast of the United States were identified as maximum decay regions of closed circulation centers.

Two objective identification and tracking schemes used to describe the distributions of extratropical cyclogenesis and cyclolysis have also been involved in this work. The first was designed by Le Truet and Kalnay (1990). Cyclones included in their statistics had to have been successfully tracked for at least three successive 6- or 12-h intervals. If a cyclone had been tracked for more than three successive time steps and could no longer be detected, it was considered a case of cyclolysis. The scheme was applied to two 50-day Goddard Laboratory for Atmospheres analyses, one beginning in January, the other in June, for the First Global Atmospheric Research Program Global Experiment year (Baker 1983). Results from the analysis showed that the North Sea and the north Pacific Ocean from south of Alaska to north of Japan were important areas of cyclolysis. There was a significant seasonal variation in the latitude for cyclolysis as the average latitude for cyclolysis was 60.3°N in summer and 55.9°N in winter. Another scheme, developed by Sinclair and collaborators over a period of years (Sinclair 1994, 1995, 1996, 1997; Kidson and Sinclair 1995), has yielded similar results with regard to the distribution of cyclolysis (see Fig. 9d, Sinclair 1997).

Within this rather disparate collection of prior studies, none has examined the spatial distribution of surface cyclolysis events continuously over a number of years or attempted to characterize the spectrum of rates of cyclolysis that exist in nature. Additionally, no prior study has revealed the characteristic composite tropospheric structure and evolution of rapid cyclolysis events. The multiyear study presented in this paper fills

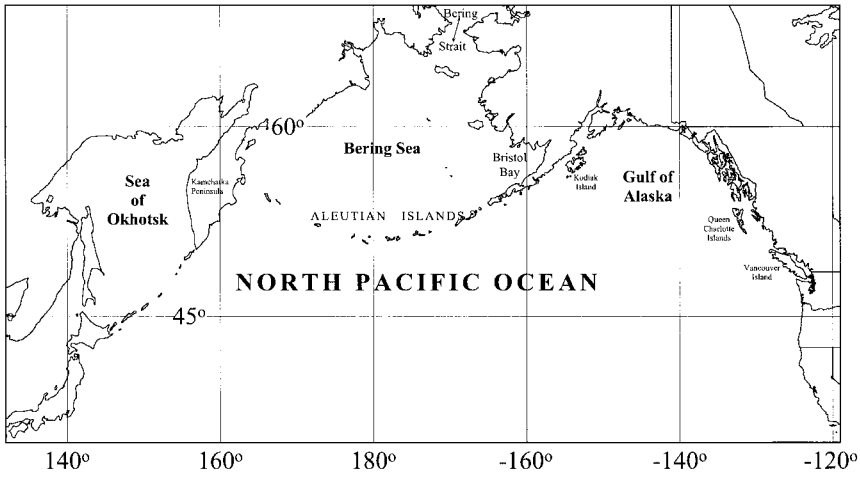

FIG. 2. Map of the North Pacific Ocean analysis region indicating the geographic locations mentioned in the text.

these gaps in knowledge by providing the most complete and comprehensive climatology to date, insights into possible interseasonal and interannual variability in cyclolysis, as well as an analysis of the composite synoptic-scale structure and evolution of rapid cyclolysis events.

3. Dataset and analysis methodology

The limited-area climatology presented here was performed over the North Pacific Ocean, Gulf of Alaska, Sea of Okhotsk, Bering Sea, and surrounding landmasses (Fig. 2) using uninitialized European Centre for Medium-Range Weather Forecasts analyses from the period July 1986 through June 1997. These data were processed using the General Meteorological Analysis Package software and were used to subjectively identify and track sea level low pressure systems in the analysis region. The reduced sea level pressure (P_{sl}) at each grid point was calculated using the twice-daily (0000 and 1200 UTC) 1000-hPa analyses of geopotential (ϕ), and virtual temperature (T_v) according to the relationship

$$P_{sl} = 1000\left(1 + \frac{\phi\Gamma}{gT_v}\right)^{g/R\Gamma}, \qquad (1)$$

where R is the gas constant for dry air (287 J kg^{-1} K^{-1}), g is the globally averaged acceleration due to gravity (9.81 m s^{-2}) at the earth's surface, and Γ is the standard atmospheric lapse rate (0.0065°C m^{-1}).

Cyclones were required to exist for at least one 12-h period to be considered for inclusion in this sample. A low pressure system was defined as a minimum in the sea level pressure field surrounded by at least one closed isobar (analyzed at 2-hPa intervals). Tropical cyclones were excluded, although once a tropical cyclone appeared to have acquired baroclinic characteristics (determined subjectively) it was included in the census. In addition, decaying systems moving from eastern Asia were not considered in our statistics until they were within 300 km of the Sea of Okhotsk and the western Pacific Ocean. Landfalling systems coming from the Sea of Okhotsk, Bering Sea, or the North Pacific Ocean were analyzed until the sea level pressure minimum was located roughly 300 km inland.

By comparing successive 12-h periods, filling rates and tracks of closed contoured minima in sea level pressure were compiled. The recorded information for each system included 12-h pressure changes, as well as the onset time, date, and position of the 12-h period of most rapid filling. Cyclones were tracked until their central pressures weakened to 1015 hPa. The location of the 12-h period of most rapid cyclolysis for each system was determined by comparing the locations of its sea level pressure minimum on the two successive maps spanning the 12 h of its most rapid filling. The midpoint of this line segment was considered the location of most rapid decay. Some slight placement errors due to the passage of time between analyses and the scarcity of data over the ocean is introduced by this method, but such errors cannot be avoided and likely do not camouflage the true nature or geographic distribution of the cyclolysis.

4. Results of cyclolysis climatology

In the course of this analysis of cyclolysis, it became apparent that a catalog of every 12-h period of cyclone filling would be an intractable problem as the sheer volume of such events is overwhelming. Evidence of this fact arose from a comprehensive analysis of decaying cyclones sampled in the 8-month period from 1 October 1986 to 31 May 1987. Every sea level low pressure system observed in the analysis region was tracked twice daily through time using the methods de-

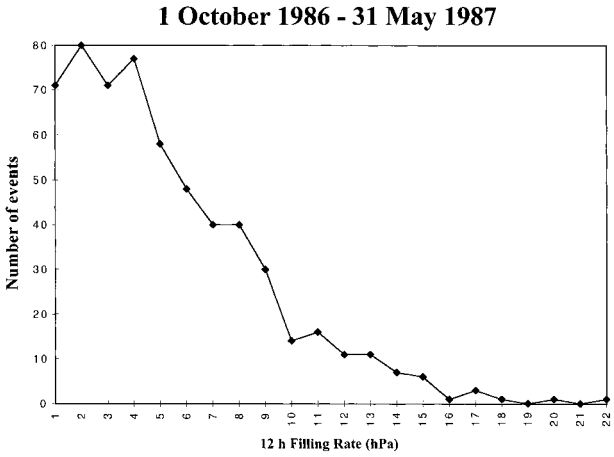

FIG. 3. Number distribution of 12-h cyclone filling rates observed in the analysis region between 1 Oct 1986 and 31 May 1987. Dots correspond to the number of 12-h filling periods observed at each discrete filling rate.

scribed in section 3. An incident of cyclolysis was noted if the pressure change at the cyclone center between successive periods was +1 hPa or greater. The number of occurrences of cyclolysis, thus defined, were totaled for the minimum filling rate of 1 hPa 12 h^{-1} up to the maximum observed filling rate of 22 hPa 12 h^{-1}. Over this 8-month period, a total of 587 filling periods, associated with 140 sampled storms, were observed. The intensity distribution of these filling rates is presented in Fig. 3. As a practical alternative to including all cyclolysis periods in the full 11-yr climatology, the analysis focused on the most rapid 20% of cyclolysis events represented by the tail of the distribution. We therefore chose to define a threshold filling period (TFP) as a 12-h period in which the sea level pressure minimum associated with a cyclone increased by at least 9 hPa. Such a definition allows for the possibility that a single cyclone may experience more than one TFP during its life cycle.

The percentile ranks of a number of 12 h filling rates in this 8 month sample are displayed in Table 1. Slightly less than one in five filling periods met the criteria for a TFP. Much less frequently observed was a filling period of at least 12 hPa in 12 h, occurring only once in every 14 cyclolytic periods. We therefore chose to define a rapid cyclolysis period (RCP) as a cyclone filling rate of at least 12 hPa 12 h^{-1}. This subjective choice provides a convenient, though not exact, symmetry with the Sanders and Gyakum (1980) *latitudinally adjusted* criteria for explosive cyclogenesis. It will be shown subsequently that the nearly 3:1 ratio between 9- and 12-hPa filling rates observed in the 8-month sample is also observed in the 11-yr climatology. Thus, the threshold value for an RCP separates a subset of rapid cyclolysis events from the much larger class of moderate ones (TFPs) upon which the climatology is based.

In this section the climatological distribution of TFPs is discussed first. The distribution of the RCP subset is then described in a similar manner. Since cyclone activity is most frequent during the cold season, our climatological ''year'' straddles that season and runs from July to June. The results of the climatology are presented in this section in two different forms; a frequency distribution and a geographical distribution. This dual presentation method is motivated by the fact that significant interannual variability exists both with regard to the number of TFPs (and cyclones with TFPs) as well as the geographical distribution of these events. The frequency distribution is presented first.

TABLE 1. Percentile ranking of all filling events occurring at or below a given filling rate from 1 Oct 1986 to 31 May 1987.

Minimum filling rate (hPa)	Percentile rank (%)
7	68.9
8	75.8
9	82.6
10	87.7
11	90.1
12	92.8

a. Frequency distribution of TFPs

The results of our 11-yr climatology show that there were 825 TFPs associated with 576 individual cyclones in the analysis region. Multiple TFPs associated with a single cyclone were observed both in consecutive 12-h periods as well as in nonconsecutive 12-h periods. A breakdown of the TFPs in the 576 cyclones is given in Table 2. Precisely two-thirds of all qualifying cyclones experienced only a single TFP while more than one in five experienced exactly two consecutive TFPs. Roughly 1 in 16 experienced three consecutive TFPs while only 1 in 72 experienced four consecutive TFPs. In this section we will present an analysis of the total frequency distribution of TFPs, a stratification of TFPs with respect to initial cyclone intensity, and a cumulative monthly distribution of TFPs.

The total number of TFPs stratified by intensity is shown in Fig. 4. Note that there is roughly a threefold decrease in the frequency of occurrence for each 3-hPa increase in filling rate. More than 65% of all TFPs occur within the range of 9–11 hPa 12 h^{-1}. The frequency distribution of TFPs in individual years of the climatology is given in Fig. 5. This portrayal of data high-

TABLE 2. Number of qualifying cyclones in the 11-yr sample with the given distribution of TFPs during the decay process.

Sequence of TFPs	Number of such cyclones
Single TFP	384
Two consecutive TFPs	127
Three consecutive TFPs	38
Four consecutive TFPs	9
Two nonconsecutive TFPs	17
Three nonconsecutive TFPs	1

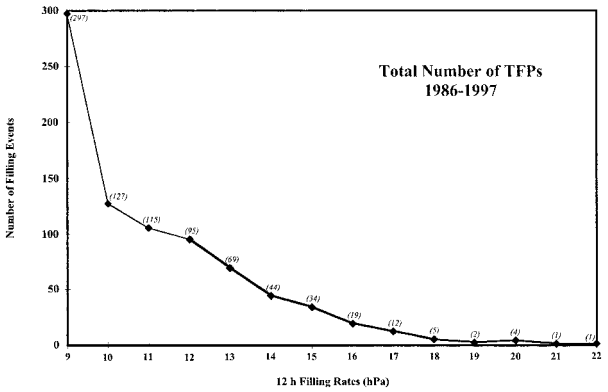

FIG. 4. Cumulative number distribution of 12-h filling rates of 9 hPa or higher over the 11-yr sample (defined as TFPs). Numbers in parentheses represent the actual number of events in each filling rate category. Light shading highlights the subset of TFPs defined as RCPs (see text for explanation).

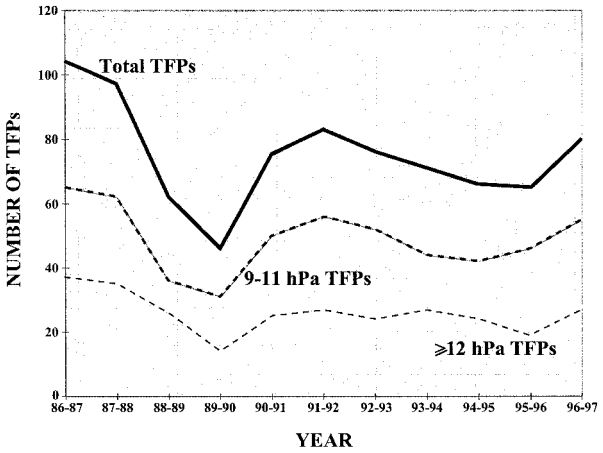

FIG. 5. Annual number of all TFP events (thick solid line) compared to the respective annual number of moderate cyclolysis events (9–11 hPa, thick dashed line) and rapid cyclolysis events (thin dashed line) for the 11-yr sample.

lights the considerable interannual variability that exists in the number of TFPs. Not surprisingly, this variability is largely reflected in the total number of TFPs of weakest intensity (9–11 hPa 12 h^{-1}).

A reasonable hypothesis regarding cyclones that experience a TFP is that they begin their periods of notable filling at a very low sea level pressure. This hypothesis is based upon the fact that intense surface cyclones experience significant lower-level mass convergence. When, on occasion, the compensating upper-level mass divergence is weaker, moderate or rapid filling may result. In order to test this hypothesis, the population of 576 cyclones containing at least one TFP was further stratified by considering their initial cyclone intensity, defined as the sea level pressure observed just before the first TFP occurs in a given cyclone. As an example, a cyclone observed to have had a sea level pressure minimum of 964 hPa immediately prior to its first TFP would be considered to have begun the cyclolysis process in the 960–969-hPa range. The results of such a partitioning are shown in Fig. 6. These results show that 189 of the 576 sampled cyclones began their filling in the 970–979-hPa range, accounting for 32.8% of cyclones with TFPs. There were 154 storms with initial cyclone intensities in the 980–989-hPa intensity range containing TFPs. Forty-one cyclones with at least one TFP began filling in the 950–959-hPa intensity range, while only nine began such decay from the 940–940-hPa range. The smaller numbers in the latter group, however, most likely reflect the increasing rarity of storms with these extremely low initial sea level pressures. Of the 576 cyclones associated with TFPs only 10 had an initial cyclone intensity of 1000–1009 hPa, while none were observed with an initial cyclone intensity exceeding 1010 hPa. Large numbers of cyclones with sea level pressure minima in the 990–1009-hPa range were found in the climatology and yet only 15.5% of all cyclones experiencing a TFP began to fill from within this range of intensity. Thus, it appears that TFPs are most likely to occur in cyclones of considerable initial intensity.

Such intense cyclones almost exclusively occur in the cold season suggesting that TFPs may well be a predominantly cold season phenomena. The monthly distribution of TFPs for the 11-yr climatology presented in Fig. 7 testifies to an obvious cold season bias for the occurrence of TFPs. In fact, more than three-quarters of all TFPs occur from November to March, and each of these months recorded more than 100 TFPs during the 11-yr climatology. Also noteworthy is the fact that the increase in TFPs transitioning from autumn to winter is much more pronounced than the decrease that occurs during the transition from winter to spring.

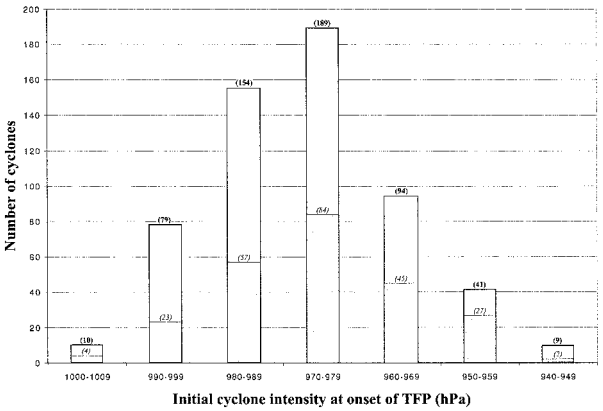

FIG. 6. Bar graph representing the initial cyclone intensity distribution for the cumulative number of cyclones that experienced a TFP. The analogous distribution for RCP cyclones is shaded gray. Numbers in parentheses represent the number of cyclones of each type (bold for TFPs, italicized for RCPs) at each initial cyclone intensity.

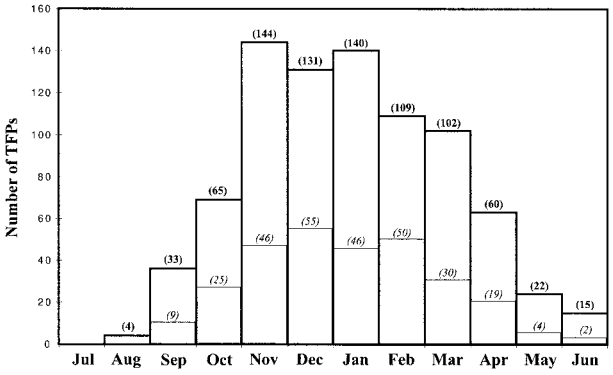

FIG. 7. Cumulative monthly distribution of TFP (RCP) events for the 11-yr sample. Number of TFP (RCP) events is in bold (italicized) numbers.

b. Geographical distribution of TFPs

Considerable variability also existed in the geographical distribution of cyclones with TFPs. In order to document this distribution, we noted the position at which each qualifying cyclone (i.e., one that experienced at least one TFP) experienced its maximum 12-h period of decay. Each such position is designated with a black dot in Fig. 8. The decision to mark only the TFP of greatest intensity for each qualifying cyclone undoubtedly yields an underrepresented distribution of cyclone decay. However, it also provides a clearer and more concise identification of the regions of most intense cyclolysis.

The interannual geographical variability of cyclolysis is considerable. Rather than display the distribution for all 11 years, only a representative couple of examples are illustrated. The frequency of TFPs in the Bering Sea varied between 1993–95 (Figs. 8a and 8b, when a large number of TFPs were documented) and 1995–97 (Figs. 8c and 8d, when very few TFPs were observed). Another example of this variability centers on the Aleutian Islands, which seemingly served as an axis of maximum TFP activity in 1993–94 (Fig. 8a) but as an axis of inactivity the following year (Fig. 8b).

The cumulative geographical distribution of maximum TFPs for the entire 11-yr climatology is presented in Fig. 9. This distribution was generated by plotting the points of maximum 12-h decay for each TFP cyclone onto a single map. The region of interest was then subdivided into 2.5° × 2.5° latitude–longitude quadrilaterals and the number of qualifying cyclones in each box was counted. These number densities were then contoured to produce Fig. 9. The analysis makes it clear that the Gulf of Alaska contained a far greater population of cyclones with TFPs than any other region in the North Pacific. A striking feature of Fig. 9 is that, not surprisingly, proximity to elevated terrain (the Coastal range of Alaska and British Columbia) apparently exerts a considerable influence on the frequency of moderate cyclolysis. Almost every location between 48° and 60°N experienced at least one qualifying cyclolysis event over the course of the 11-yr climatology. The average latitude for all qualifying cyclones in our study was 55.8°N, nearly identical to that observed by LeTruet and Kalnay (1990) in a much more limited study. Also, the distribution in Fig. 9 fortifies the earlier analyses of Roebber (1984) and Gyakum et al. (1989) (Figs. 1b,d).

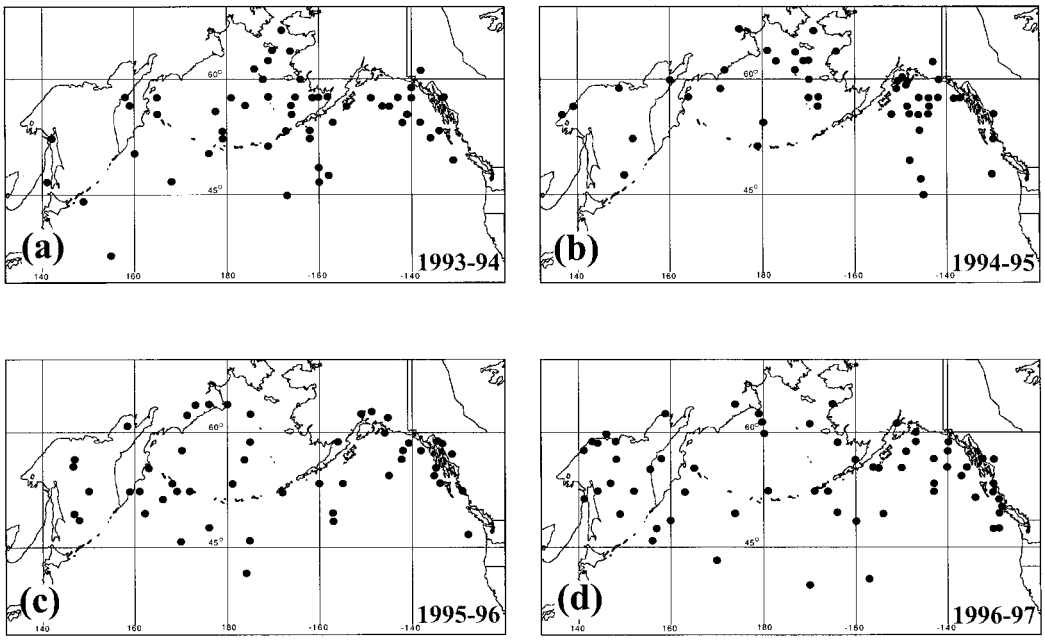

FIG. 8. Geographical distribution of maximum decay positions (black dots) of TFP cyclones observed in (a) 1993–94, (b) 1994–95, (c) 1995–96, and (d) 1996–97.

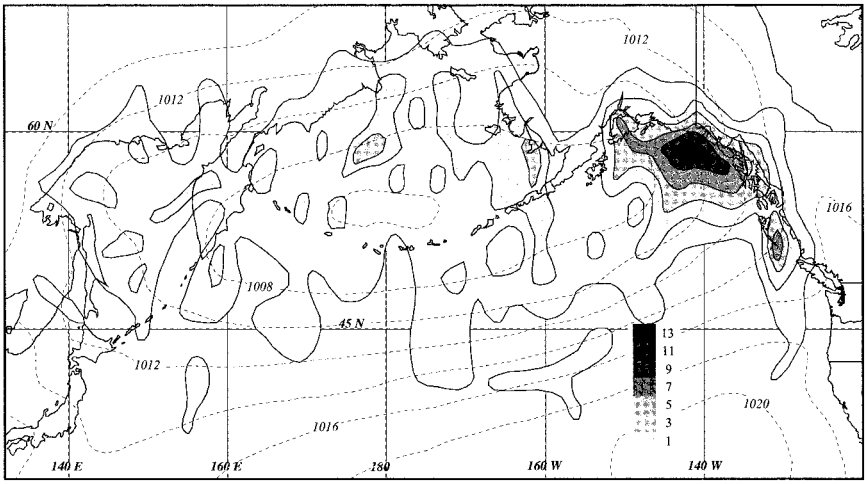

FIG. 9. Cumulative areal number distribution of TFP cyclones from 1986 to 1997. Thin dashed lines are the 11-yr average sea level isobars labeled in hPa and contoured every 2 hPa.

c. Frequency of RCPs

In the 11-yr sample there were 286 RCPs associated with 242 distinct cyclones. In contrast to the fairly high number of cyclones exhibiting multiple TFPs, only 44 of the 242 rapidly decaying cyclones (18%) exhibited multiple RCPs. The distribution of initial cyclone intensity for all RCP storms is presented in Fig. 6. The storms that compose this population did not necessarily begin the decay phase with an RCP but rather had at least one RCP during the decay process. The distribution for RCP storms is nearly symmetric around the 970–979-hPa range (slightly skewed toward higher pressure intervals). The distribution for non-RCP storms in the sample is much more obviously skewed toward higher pressure intervals. The RCPs are less broadly distributed by month than the TFPs (Fig. 7) and exhibit a slightly more abrupt seasonal transition than do the TFPs. The RCPs are still a predominantly cold season phenomena with nearly 70% of all events occurring from November to February.

It is interesting to consider what percentage of TFP cyclones in a given initial cyclone intensity range experience an RCP during their decay stage. Such percentages can be gleaned from Fig. 6. Excluding the 1000–1009- and 940–949-hPa ranges (as 10 or fewer cyclones populated each of these ranges), it is clear that the percentage of TFP storms that experience an RCP increases steadily as the initial cyclone intensity increases. Thus, more intense cyclones that are decaying at at least a moderate rate run a greater risk of experiencing a period of rapid decay than weaker, moderately decaying storms.

d. Geographical distribution of RCPs

A sample of the geographical distribution of cyclones experiencing RCPs is shown in Fig. 10. Analogous to the portrayal in Fig. 8, each square represents the position at which each qualifying cyclone experienced its maximum 12-h period of decay. The RCP cyclones demonstrate a similar interannual variability as the larger population of TFP cyclones. Note, for instance, the substantial differences in the Bering Sea between the successive years 1988/89 and 1989/90 (Figs. 10a,b). Also, rapid cyclolysis in the Gulf of Alaska was quite densely distributed in 1992/93 but rather sparsely so just four years later (Figs. 10c,d).

The cumulative distribution of RCPs over the 11-yr climatology is shown in Fig. 11. Constructed in the same manner as Fig. 9, the analysis reveals that the Gulf of Alaska is the most likely portion of the North Pacific to host a rapid cyclolysis event. The Bering Sea represents the only other spatially coherent region in which rapid cyclolysis is common and widely distributed. The western and central North Pacific, on the other hand, experienced relatively few cyclones with RCPs. The average latitude for all RCPs in the sample was 56.3°N, half a degree farther north than that of the larger class of TFPs.

e. Interannual variability of cyclolysis and ENSO

As previously shown, analysis of the year to year distribution of decaying surface cyclones reveals the existence of considerable interannual variability in both the total number of events and their spatial distribution. It is tempting to suggest that some link may exist between this observed interannual variability and recognized global-scale climate anomalies.

The most widely acknowledged coupled ocean–atmosphere phenomenon responsible for global climate variability on the interannual timescale is the ENSO. In the Northern Hemisphere winter, El Niño events (the warm phase of ENSO) are associated with a strong

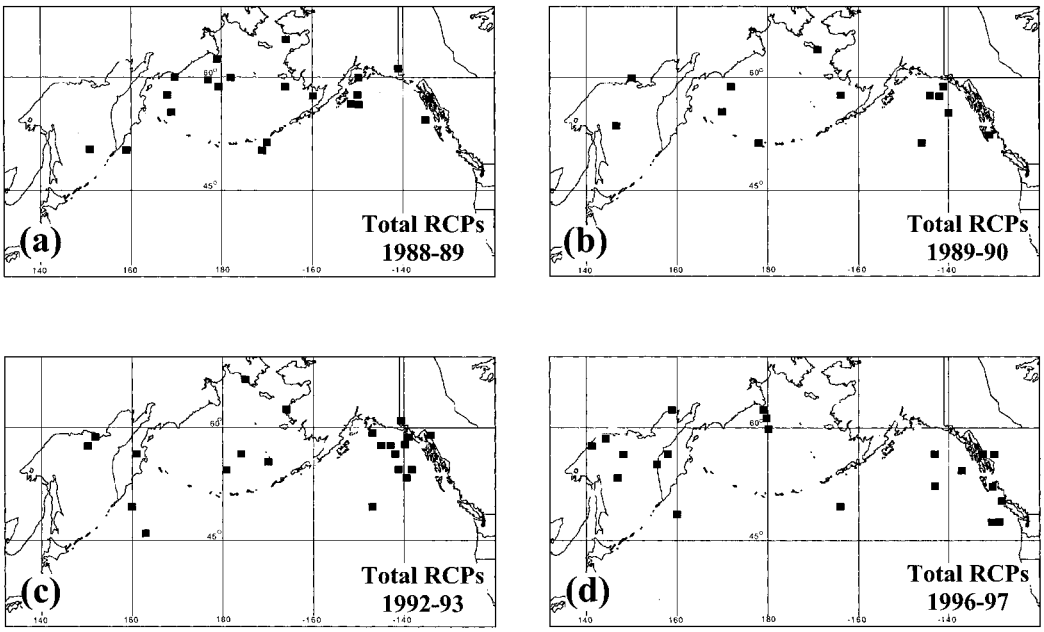

FIG. 10. Geographical distribution of maximum decay positions (black dots) of RCP cyclones observed in (a) 1988–89, (b) 1989–90, (c) 1992–93, and (d) 1996–97.

trough and ridge teleconnection pattern (Horel and Wallace 1981), known as the Pacific–North American pattern (Wallace and Gutzler 1981), which usually brings clouds and rain to the southwestern United States and northwest Mexico while the Midwest and Pacific Northwest are typically drier and slightly warmer. The cold phase of ENSO, La Niña, often results in a more zonal jet in the Northern Hemisphere winter. A consequence of this zonal jet is a warmer than average southeastern United States and a colder and wetter northwestern United States.

The multivariate ENSO index (MEI) is a diagnostic tool used to monitor the magnitude and phase of ENSO and is based on six primary atmospheric and oceanic variables over the tropical Pacific Ocean. These six variables are sea level pressure, zonal and meridional components of the surface wind, sea surface temperature, surface air temperature, and fractional cloud cover. These six components are combined to compute the MEI for each of 12 sliding bimonthly periods (December–January, January–February, . . . , November–December) (Wolter and Timlin 1993). A positive MEI corresponds to El Niño conditions while a negative MEI corresponds to La Niña conditions.

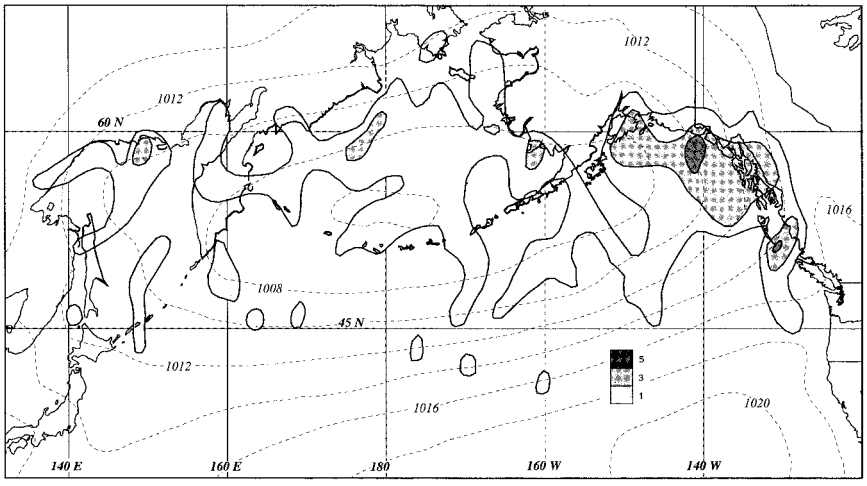

FIG. 11. Cumulative areal distribution of RCP cyclones from 1986 to 1997. Thin dashed lines are the 11-yr average sea level isobars labeled in hPa and contoured every 2 hPa.

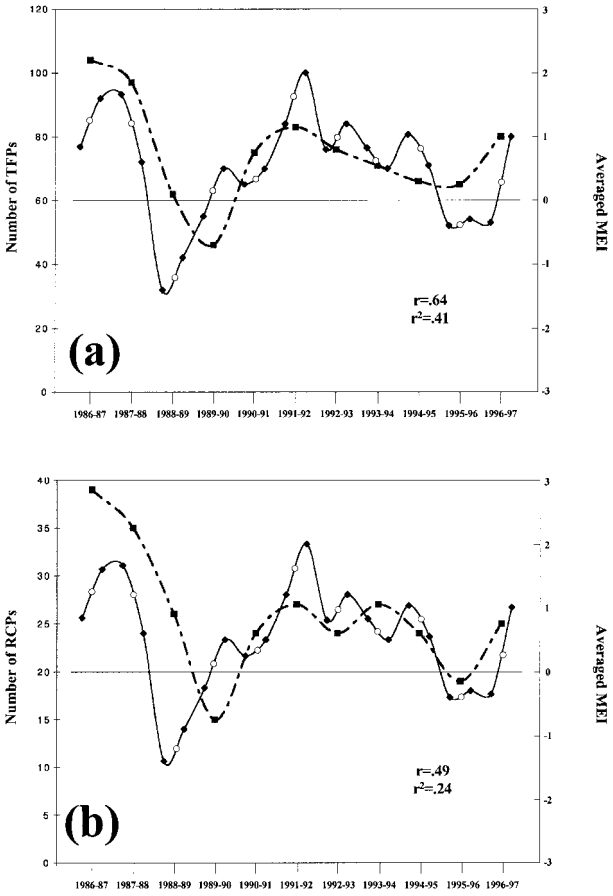

FIG. 12. (a) Time series of the number of TFP cyclones (gray squares) in each year of the 11-yr sample contoured as a dashed line. Time series of MEI (see text) is contoured as a solid line. Black squares represent the MEI value averaged over 6-month periods centered on Apr and Oct of each year. Open circles represent the mean MEI for each climatological year. The linear correlation coefficient, *r*, relates mean annual MEI to the number of TFPs in each year of the time series. (b) As for (a) except dashed line represents a time series of annual number of RCP cyclones and r relates this number to the mean annual MEI.

The observed interannual variability of moderate cyclolysis in the north Pacific Ocean appears to be related to the ENSO phenomenon. Figure 12a shows this relationship graphically by portraying the MEI and the annual number of TFPs. The squares in the MEI time series (solid line) represent the MEI value averaged over 6-month periods centered on April and October of each climatological year. The open circles on the MEI time series are the mean of the averaged April and October MEI values for a given climatological year. It is these values whose linear correlation with the number of TFPs in each year is given by the correlation coefficient, *r*. A correlation coefficient of 0.64 is fairly large and indicates that nearly 41% of the variation in the number of TFPs may be accounted for by a linear relationship with ENSO as measured by the MEI. Rapid cyclolysis was also compared with the MEI to determine if some correlation exists between these more extreme cyclolysis events and ENSO. Figure 12b compares the averaged MEI to the number of RCPs over the 11-yr study. The *r* value for these data is lower, 0.49, suggesting that 24% of the variation in the number of RCPs may be accounted for by a linear relationship with ENSO as measured by the MEI. Finally, a one-sided Student's t-test indicates that these correlations are significant at the 95% confidence level.

Thus far, statistical information regarding the distribution of moderate to rapid cyclolysis events in the north Pacific Ocean has been presented. In an attempt to better understand the physical mechanisms that contribute to cyclolysis in the North Pacific basin, a composite analysis of the structural evolution of decaying cyclones is presented in the next section. To make the problem slightly more tractable while preserving the essence of the physical processes involved, we consider only a subset of all TFP cyclones, namely, those that experienced a single RCP.

5. Composite structure of RCP cyclones

In our 11-yr sample, there were 200 individual cyclones that experienced a single RCP. Although perusal of this set of storms revealed considerable intercase variability in large-scale structure and evolution, there were some common features as well. In an effort to isolate these common elements of single RCP cyclones in the North Pacific Ocean, this section presents and discusses the results of analysis of the composite structure and evolution of such cyclones in the 11-yr sample. For each discrete single RCP cyclone in the sample, we define $T = 0$ as the *beginning* of the 12-h period during which the RCP for a given cyclone occurred. This designation allows the discussion of the composite RCP to be normalized to a common decay following time. For each single RCP cyclone in the sample, three days of data on either side of $T = 0$ were considered. In the course of the subsequent presentation, reference will be made to three other analysis times; $T - 24$ h, $T - 12$ h, and $T + 12$ h, which refer to the moments 24 and 12 h *before*, and 12 h *after*, the initiation of rapid decay, respectively.

In order to take account of the wide spatial distribution and temporal evolution of the set of single RCP cyclones, the following compositing procedure was followed. For each analysis time, the sea level pressure minimum of each single RCP cyclone was located.[1] Then a grid box with dimensions 40° × 100° (repre-

[1] Of the 200 single RCP cyclones, some data in the 6 days centered on $T = 0$ was missing for 13 of them. These 13 storms were excluded from the composite. Of the remaining 187, the locations of the sea level pressure minimum of 7 were difficult to unambiguously identify at $T + 12$ h. These 7 storms were also excluded from the composite as a result.

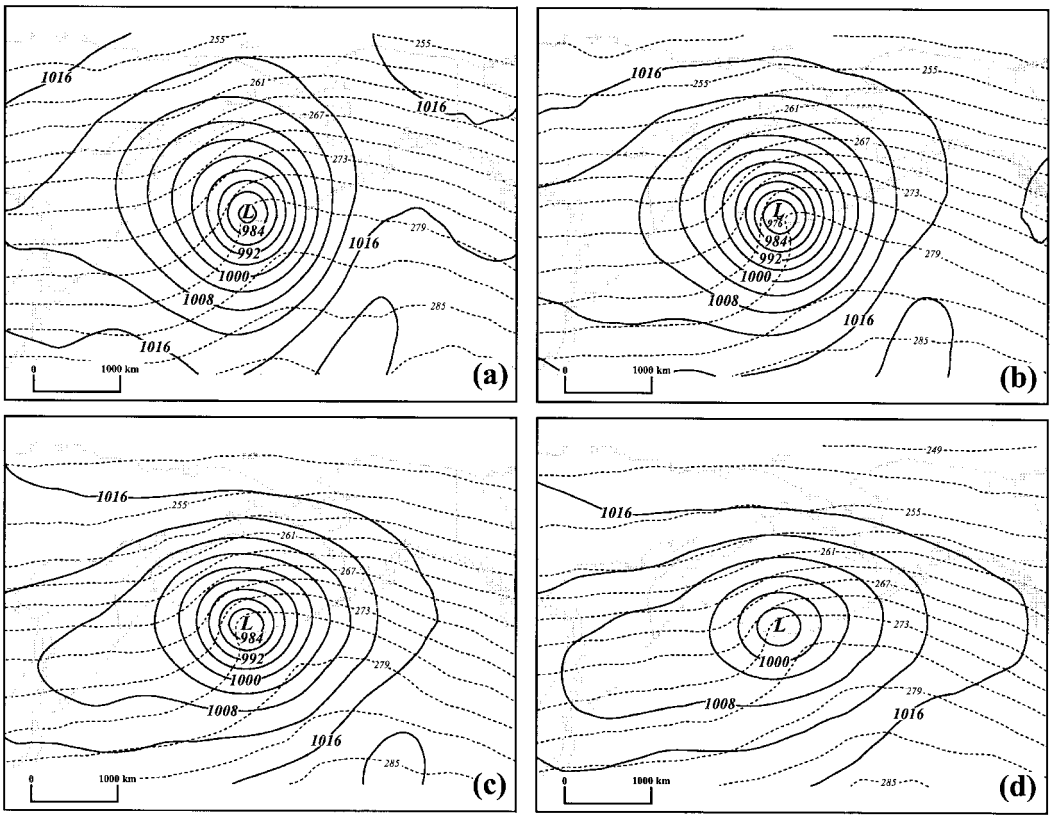

FIG. 13. (a) Sea level isobars (solid lines) and 1000-hPa potential temperature (dashed lines) for the composite RCP cyclone at $T - 24$ h (see text for explanation). Isobars are labeled in hPa and contoured every 4 hPa. Potential temperature labeled in K and contoured every 3 K. The map background provides a scale only and implies nothing about the geographic distribution of the storms composing the composite cyclone. (b) As for (a) but for composite time $T - 12$ h. (c) As for (a) but for composite time $T = 0$. (d) As for (a) but for composite time $T + 12$ h.

senting a 17×41 array of grid points) centered on the position of the sea level pressure minimum at that time was saved for each cyclone. The composite distribution of a given variable at each analysis time was then constructed by taking the 180-case average of that variable at each of the 697 grid points within the latitude–longitude grid box and then contouring those gridpoint values. The results are displayed on a map of the Pacific basin centered on 56.3°N (the average filling latitude for all RCPs). The geographical map is used as a background in order to provide a representative scale to the composite structures in the analysis; it is *not* meant to imply anything about the actual geographical distribution of the composite RCP cyclone.

a. RCP cyclone evolution from a traditional quasigeostrophic perspective

The composite evolution of sea level pressure at 12-h intervals from $T - 24$ h to $T + 12$ h is shown in Fig. 13. It is immediately clear that RCP cyclones generally undergo a period of intensification between $T - 24$ h and $T - 12$ h (Figs. 13a,b). Though the composite method employed here undoubtedly smoothes away the details of lower-tropospheric frontal structure to a large degree, it is still apparent that this development period is associated with progress toward occlusion as evidence for the development of the characteristic lower-tropospheric occluded thermal ridge appears in Fig. 13b.

In the next 12 h, some robust filling occurs in the sea level pressure field as the 1000-hPa thermal field (which becomes cooler at the sea level pressure minimum) suggests a continuation of the occlusion process (Fig. 13c). By the end of the first 12 h of rapid decay, the sea level pressure minimum has increased dramatically and the composite thermal structure at 1000 hPa has relaxed as well. Note that, by this time, the cyclone center is located deeper into the cold air north and west of the triple point (approximately the poleward bulge of the 276 K isentrope) (Fig. 13d).

This surface evolution is accompanied by an equally compelling composite evolution at 500 hPa (Fig. 14). At $T - 24$ h a well-developed, slightly negatively tilted trough in the geopotential height exists in the composite with the sea level pressure minimum located just downstream of the maximum curvature region (Fig. 14a). Twelve hours later, at $T - 12$ h, the upper trough axis has become more negatively tilted and the sea level

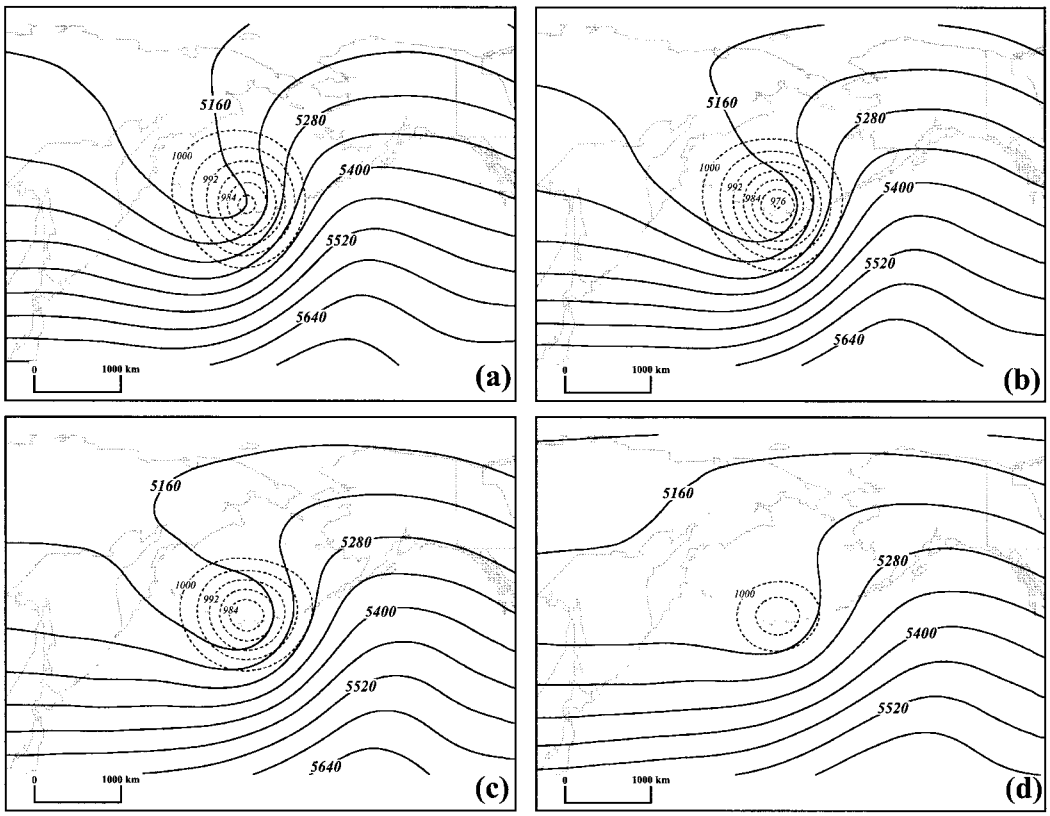

FIG. 14. (a) 500-hPa geopotential height (dark solid lines) and sea level isobars (light dashed lines) for the composite RCP cyclone at $T - 24$ h. Geopotential height is labeled in m and contoured every 60 dm. Isobars are labeled in hPa and contoured every 4 hPa to a maximum of 1000 hPa. (b) As in (a) but for composite time $T - 12$ h. (c) As in (a) but for composite time $T = 0$. (d) As in (a) but for composite time $T + 12$ h.

pressure minimum has drawn closer to the trough axis (Fig. 14b), again, characteristic of an occluding cyclone. By $T = 0$ the sea level pressure minimum lies directly beneath the 500-hPa geopotential height minimum of an even more negatively tilted trough (Fig. 14c). An astounding transformation in the geopotential height field occurs in the next 12 h, during the RCP. The radius of curvature of streamlines increases dramatically while the 500-hPa geopotential gradient weakens south of the sea level pressure minimum (Fig. 14d). This rapid flattening of the 500-hPa trough–ridge couplet, which had been amplifying up to the commencement of cyclone decay, is suggestive of a rapid decrease in the upper-tropospheric divergence downstream of the upper trough axis (i.e., to the northeast of the sea level pressure minimum). Such a circumstance, occurring immediately after the surface cyclone reaches its maximum intensity, provides the key ingredient for the subsequent rapid cyclolysis at the surface. As the surface cyclone reaches its greatest intensity, presumably so does the lower-tropospheric mass convergence into it, forced by friction in the boundary layer. With the abrupt reduction in cyclonic curvature and, consequently, in the mass divergence aloft, the accumulating mass in the lower troposphere is less efficiently evacuated from the column and the sea level pressure (SLP) rises rapidly as a result. It is interesting to note that the antecedent decay of the upstream ridge evident in Fig. 14 is consistent with the recent analyses by Chang (2000) concerning wave packet propagation and its role in the cyclone life cycle.

Additional evidence for the effect of rapid changes in the mid- and upper troposphere on surface cyclone decay is given in Fig. 15, which shows the composite evolution of the 1000–500-hPa column averaged **Q**-vector divergence. At $T - 24$ h significant column averaged **Q**-vector convergence was in place just north of the composite SLP minimum (Fig. 15a). During the subsequent 12 h of development, the **Q**-vector convergence maximum remained vigorous (Fig. 15b) and similarly positioned with respect to the SLP minimum. Convergence of the **Q** vector is associated with upward vertical motion (Hoskins et al. 1978) and therefore Figs. 15a and 15b are consistent with the development of the composite RCP cyclone observed in this predecay phase of the life cycle. At the commencement of cyclone decay ($T = 0$, Fig. 15c) the position of the SLP minimum nearly straddled the dipole of **Q**-vector convergence/divergence. As the amplitude of the upper wave rapidly waned in the ensuing 12 h, the magnitudes of the **Q**-vector convergence/divergence were dramatically reduced.

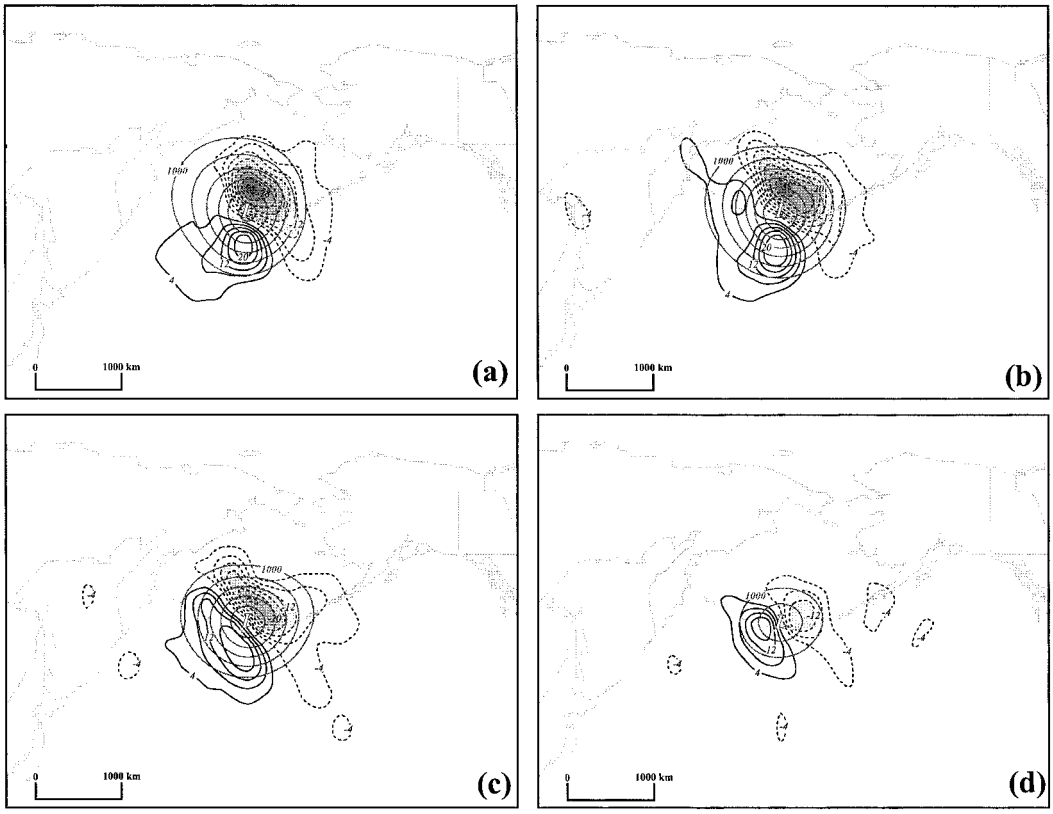

FIG. 15. (a) 1000–500-hPa column averaged $-2\nabla \cdot \mathbf{Q}$ and sea level pressure for the composite RCP cyclone at $T - 24$ h. **Q**-vector convergence (dashed lines) contoured and shaded in units of m kg^{-1} s^{-1} every -4×10^{-16} m kg^{-1} s^{-1} beginning at -4×10^{-16} m kg^{-1} s^{-1}. **Q**-vector divergence (solid lines) contoured in units of m kg^{-1} s^{-1} every 4×10^{-16} m kg^{-1} s^{-1} beginning at 4×10^{-16} m kg^{-1} s^{-1}. Sea level isobars (gray solid lines) labeled in hPa and contoured every 4 hPa with a maximum of 1000 hPa. (b) As in (a) but for composite time $T - 12$ h. (c) As in (a) but for composite time $T = 0$. (d) As in (a) but for composite time $T + 12$ h.

By $T + 12$ h the magnitude of the **Q**-vector divergence was larger than the convergence. The rapidly filling SLP minimum was located at the center of this divergence–convergence couplet (Fig. 15d).

Thus, we suggest that the decay of the composite RCP cyclone resulted from significant decay of the upper-level wave in combination with lower-tropospheric mass convergence in the friction layer. The magnitude of the frictional lower-tropospheric mass convergence was controlled by the intensity of the sea level pressure minimum and, thus, was maximized just before cyclone decay began. With the deamplification of the upper-tropospheric trough–ridge couplet, forcing for upward vertical motion, which normally sustains surface cyclone intensity, was abruptly diminished as indicated by the rapid reduction in magnitude of the column averaged $\nabla \cdot \mathbf{Q}$ during decay. Every intense surface cyclone experiences frictionally induced mass convergence in the boundary layer, but only a small subset of these storms decay rapidly. It is reasonable to conclude, therefore, that the distinguishing physical factor in rapid cyclolysis events is the significant and abrupt decay of the upper-level trough–ridge structure. The composite analysis also reveals that these decay events are characterized by an upper-level wave that, though initially located to the west of the surface cyclone, is eventually located to the east of the surface feature. This observed change in the vertical phase tilt of the upper and lower circulation centers placed the surface cyclone center between the weakening upward and downward vertical motion forcing centers. By the time of most rapid decay there was no net forcing for upward vertical motion over the cyclone center. The evolution of this phase tilt and its role in the composite rapid cyclolysis process are next considered from the complementary potential vorticity (PV) perspective.

b. PV perspective of the composite evolution

In their comprehensive review of potential vorticity and its applications to the diagnosis of midlatitude weather systems, Hoskins et al. (1985) suggested that baroclinic development results from the favorable superposition of a tropopause level PV anomaly and a near-surface potential temperature (θ) anomaly of like sign. When the tropopause PV anomaly is located up-

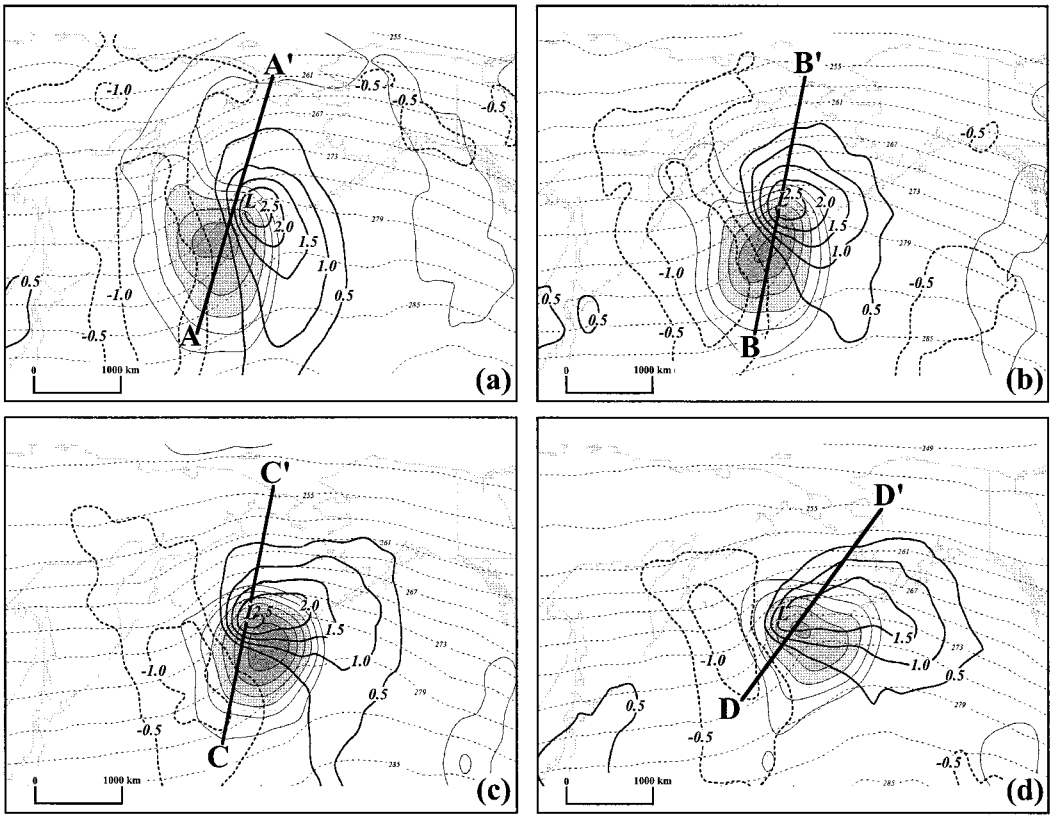

FIG. 16. (a) 200–300-hPa positive perturbation potential vorticity (PV), and 1000 hPa potential temperature (θ) perturbations for the composite RCP cyclone at $T - 24$ h. PV perturbations shaded at intervals of 0.25 PVU (1 PVU $= 10^{-6}$ m^2 K kg^{-1} s^{-1}) beginning at 0.25 PVU. Thick solid (dashed) lines are positive (negative) 1000-hPa θ perturbations labeled in K and contoured every 0.5 (-0.5) K beginning at 0.5 (-0.5) K. Thin dashed lines are composite 1000-hPa θ labeled and contoured as in Fig. 13. See text for explanation of how perturbation quantities are calculated. Cross section along line A–A′ is shown in Fig. 17a. (b) As in (a) but for composite time $T - 12$ h. Cross section along line B–B′ is shown in Fig. 17b. (c) As in (a) but for composite time $T = 0$. Cross section along line C–C′ is shown in Fig. 17c. (d) As in (a) but for composite time $T + 12$ h. Cross section along line D–D′ is shown in Fig. 17d.

shear (i.e., upwind in a thermal wind sense) of the surface θ anomaly, the circulation associated with each can act to lock them into a favorable westward tilted structure that allows the circulation associated with each anomaly to amplify the other. It was also suggested that superposition of one anomaly on the other results in an enhanced circulation as the discrete circulations associated with the two anomalies sum to a grander total.

In this portion of the analysis, composite *anomalies* in the 200–300-hPa layer averaged PV and 1000-hPa θ were considered. The anomalies for an individual case were calculated using a 6-day time mean, centered at $T = 0$, for that case. This single-case time mean was then subtracted from the instantaneous PV (θ) values for that case at each analysis time to generate single-case anomalies at each time. The 180 single-case anomalies at a given time were then averaged to get the composite anomaly at that time.

Figure 16 shows the positive near-tropopause PV anomalies and the 1000-hPa θ anomalies for four times in the composite evolution of the RCP cyclones. At $T - 24$ h (Fig. 16a) a modest, rather elongated composite upper PV anomaly was located just upstream of the 1000-hPa thermal ridge that represented the positive 1000-hPa θ anomaly (the 1000-hPa θ is also included in Fig. 16). Note the SLP minimum at this time was located near the point where the upper PV and lower θ anomalies intersected in the horizontal plane. It is clear that the upper PV anomaly at $T - 24$ h was positioned so that its associated circulation was acting to intensify the lower boundary θ anomaly. There was no significant vertical superposition of the two anomalies at this time.

Twelve hours later, at $T - 12$ h, the upper PV feature was slightly more anomalous and the circulation associated with it had further distorted the 1000-hPa θ field, rotating the θ anomaly in the process (Fig. 16b). At this time the SLP minimum was more intense, reflective of the more substantial superposition of the upper and lower PV anomalies. The requisite phase tilt for further amplification was still evident as the upper anomaly center remained to the southwest of the lower θ anomaly. By $T = 0$ the lower θ anomaly remained robust

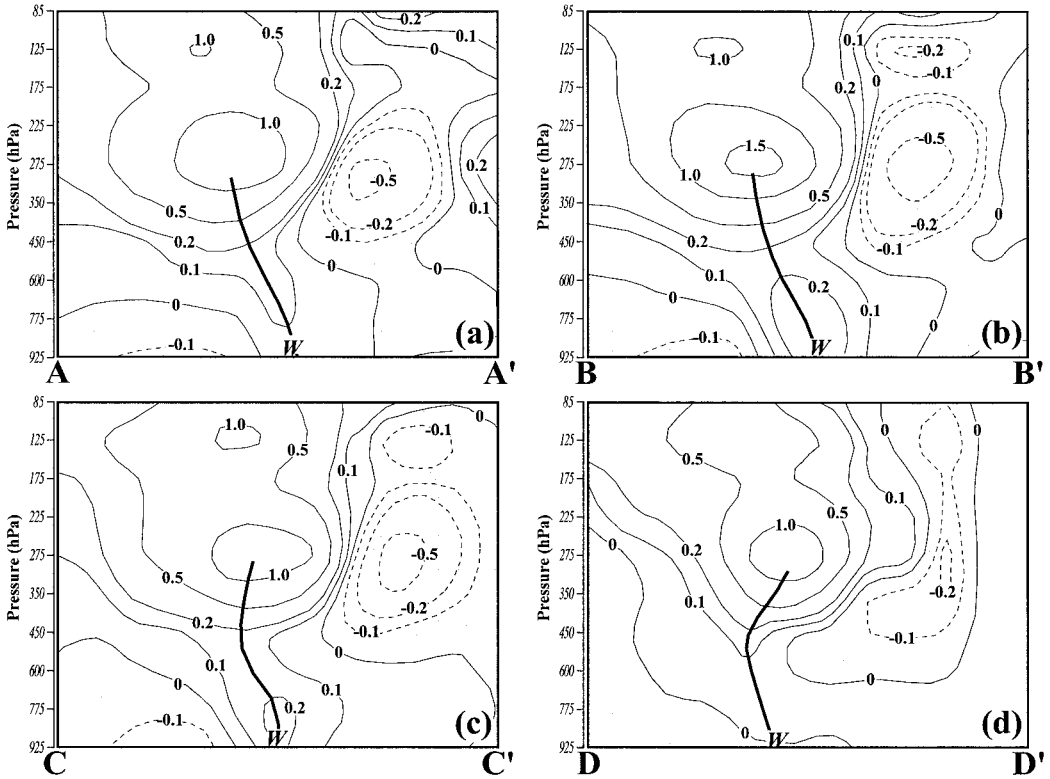

FIG. 17. (a) Vertical distribution of the composite, perturbation PV along line A–A′ in Fig. 16a for composite time $T - 24$ h. Unshaded (shaded) area represents positive (negative) PV perturbations, labeled in PVU and contoured with solid (dashed) lines. Thick solid line is the axis of maximum PV perturbation in the vertical. ''W'' indicates position of the 1000-hPa θ anomaly. (b) As in (a) but for composite time $T - 12$ h along line B–B′ in Fig. 16b. (c) As in (a) but for composite time $T = 0$ along line C–C′ in Fig. 16c. (d) As in (a) but for composite time $T + 12$ h along line D–D′ in Fig. 16d.

and had rotated farther to the west as the near-tropopause PV feature became more anomalous (Fig. 16c). The upper PV and lower θ anomalies were nearly completely superposed at this time, though the circulation associated with the upper anomaly was no longer positioned so as to amplify the near-surface θ anomaly. Finally, at $T + 12$ h the upper PV anomaly had substantially weakened, as had the lower boundary θ anomaly (Fig. 16d). By $T + 24$ h (not shown) the upper PV anomaly had shriveled to less than half of its value at $T + 12$ h and the 1000-hPa θ anomaly also continued to erode with its maximum heading south-southeastward away from the upper PV feature.

The evolution of the vertical phase tilt of the composite disturbance is portrayed in Fig. 17 using vertical cross sections of PV anomalies cut along the lower-tropospheric shear in the vicinity of the maximum upper-level PV anomaly at each of the four analysis times. These sections were constructed, one for each analysis time, by averaging all 180 single-case PV anomaly cross sections at the given analysis time along the indicated lines in Fig. 16. It is clear that at $T - 24$ h the axis of maximum positive PV perturbation had an upshear tilt with height (Fig. 17a). As the composite cyclone developed in the ensuing 12 h, the tilt remained upshear while a more substantial lower-tropospheric PV anomaly developed (Fig. 17b). By the onset of cyclone decay the positive PV anomaly axis exhibited a slight but noticeable downshear tilt with height in the mid- and upper troposphere while the magnitude of the lower-tropospheric PV anomaly had decreased (Fig. 17c). Finally, at $T + 12$ h the positive PV anomaly axis exhibited strong downshear tilt in the mid- and upper troposphere and extremely small values in the lower troposphere (Fig. 17d). Also, by this time the tropopause-level PV anomaly was downshear of the surface warm anomaly. Such a vertical structure is characteristic of decaying baroclinic disturbances; as the PV anomalies become ''attenuated'' (i.e., move farther apart from one another) the system as a whole weakens. The rapidity of the increase in the along-shear slope of the positive PV anomaly axis in the mid- and upper troposphere between $T = 0$ and $T + 12$ h would appear to be a gauge of the rapidity of surface cyclolysis.

Thus, the composite period of rapid decay at sea level began with the upper-level PV and near-surface θ anomalies nearly vertically superposed. A slight downshear phase tilt to the mid- and upper-tropospheric PV anom-

aly axis was noted. By $T + 12$ h the upper PV anomaly was located downshear of the near surface warm anomaly. This downshear tilt was conducive to a deamplification of both anomalies during the 12-h period of rapid decay. It is hypothesized that the deintensification of these anomalies, combined with the acquisition of a slightly downshear tilt, resulted in a rapid decrease in circulation associated with the SLP minimum. This decrease in circulation was manifest as a rapid rise in SLP: a rapid cyclolysis period. We are currently undertaking a piecewise PV inversion analysis to quantitatively examine aspects of the evolution suggested by the present analysis.

6. Discussion and conclusions

Understanding of the life cycle of extratropical cyclones stands as one of the major achievements of synoptic–dynamic meteorology in the past century. Comprehensive knowledge of this life cycle must account not only for the origin of cyclones (cyclogenesis) and the structural transformations they undergo during development, but also for their inevitable decay (cyclolysis). Historically, the process of cyclolysis has been little studied and thus our knowledge of the cyclone life cycle, though considerable, remains incomplete.

As a step toward remedying this situation, in this paper we have examined a continuous 11-yr sample of extratropical cyclones in the North Pacific Ocean in order to 1) construct a synoptic climatology of moderate to rapid surface cyclolysis in the region, and 2) examine the composite synoptic-scale evolution of particularly extreme cyclolysis events. The climatology presented here was constructed by manually identifying and tracking all closed contour minima in sea level pressure according to a method outlined in section 3. The powerful and more flexible objective cyclone identification and tracking method, based upon areal measure of circulation, developed by Sinclair and collaborators (Sinclair 1994, 1995, 1996, 1997; Kidson and Sinclair 1995) was not available for our analysis. Their method was developed in part to minimize several potential pitfalls of using sea level pressure minima to *objectively* track cyclones, such as the biased counting of slow moving and/or deep cyclones. The labor intensive, manual perusal of data employed here ensures that every sea level pressure minima that was resolved by the 12-h data was assessed to determine whether or not it met the filling criteria necessary to be included in the climatology.

An additional potential problem arises when drastic changes in minimum sea level pressure are not accompanied by circulation changes. Sinclair (1997) illustrates a case in which a cyclonic disturbance crosses a substantial climatological sea level pressure gradient and experiences a rapid reduction in its central pressure, suggestive of rapid development (see Fig. 3 of Sinclair 1997). Despite this apparent development, the intensity of this storm, as measured by circulation, remained constant throughout the episode. This type of error, however, seems particularly likely to occur in the Southern Hemisphere, where the winter is characterized by a significant climatological sea level pressure gradient between 40° and 60°S. In the present study, cyclone propagation across the climatological sea level pressure gradient in the Gulf of Alaska (isobars describing this field are included in Figs. 9 and 11) accounts for, at most, 3 hPa of filling in 12 h, based upon climatological cyclone velocities in the area obtained from Fig. 9c of Sinclair (1997). Thus, the methodical, subjective identification and tracking method used in this study does not suffer from the above concerns.

Based upon a census of all 12-h periods of Lagrangian sea-level pressure rise in a single season, we defined a threshold filling period, or TFP (rapid cyclolysis period, or RCP), as a 12-h period during which the sea level pressure minimum associated with a cyclone increased by at least 9 (12) hPa. The TFP events were considered moderate cyclolysis events and were found to be relatively rare. The even less common RCP events were considered examples of rapid cyclolysis. The frequency and geographical distribution of TFP and RCP cyclones exhibited considerable interannual variability with nearly all instances occurring north of 45°N. The cumulative geographical distribution of TFPs and RCPs revealed that both exhibited a primary maximum in the Gulf of Alaska and along the coast of British Columbia with a secondary maximum in the Bering Sea. It was revealed that cyclones that experience moderate to rapid cyclolysis tend to begin their decay phases at very low sea level pressures while the increase in monthly frequency of these cyclones was most abrupt during the autumnal transition to winter, especially so for TFP cyclones. Additionally, a considerable correlation between the number of TFP/RCPs in a given year and the strength and phase of the El Niño–Southern Oscillation (ENSO) as measured by the annual averaged multivariate ENSO index (MEI) suggests that TFP–RCP cyclones are more numerous in the northeast Pacific during an El Niño year.

In their examination of surface cyclone and anticyclone tracks, Wallace et al. (1988) noted that lower-tropospheric decay over the North Pacific Ocean occurred in the exit regions of elongated maxima in the variance of the high-pass filtered geopotential, what they termed baroclinic waveguides, referred to as ''storm tracks'' by Blackmon et al. (1977). Not surprisingly, the TFP and RCP frequency maxima documented in the present study occur predominantly in the same region. A similar baroclinic waveguide exists in the Atlantic Ocean extending from the east coast of North America to near Iceland (see Fig. 19a of Wallace et al. 1988). A clear extension of the present study is to compile a similar synoptic climatology of moderate to rapid cyclolysis at the end of the North Atlantic waveguide. Given that its eastern end is not nearly as mountainous as the eastern end of the Pacific storm track, such a

companion analysis would help determine the relative influence of surface characteristics versus large-scale dynamics in forcing these extreme cyclolysis events. Construction of this synoptic climatology is currently under way.

In an attempt to better understand the synoptic settings within which RCP cyclones decay we considered the composite structure and evolution of 180 single RCP cyclones observed over the 11-yr period. This analysis revealed that a period of considerable intensification during the day prior to the onset of rapid decay was characteristic of these cyclones. The development was associated with an intensifying, increasingly negatively tilted 500-hPa trough upstream of the surface cyclone with significant column averaged **Q**-vector convergence to the northeast of the surface cyclone. The rapid decay was found to be coincident with an abrupt change in the 500-hPa flow manifested as a sudden decrease in amplitude of the geostrophic vorticity and the radius of curvature of the streamlines. This change was associated with an equally abrupt change in the magnitude of $\nabla \cdot \mathbf{Q}$ in the column above the surface cyclone. Thus the composite analysis suggests that large-scale dynamical processes play a *primary* role in producing rapid cyclolysis events. A companion analysis of the composite evolution from a PV perspective revealed that a weakening of the upper- and lower-level PV anomalies and acquisition of a downshear vertical phase tilt were central to the subsequent rapid decay. The role of diabatically generated midtropospheric PV in the process of cyclolysis will be considered in future work.

In the course of constructing the composite analysis we noted that there appear to be differences between the composite structures of RCP cyclones observed in the Gulf of Alaska and those found in the Bering Sea. The physiography of these two regions is quite different as landfalling cyclones encounter mountainous terrain in the Gulf of Alaska region but considerably flatter terrain in the Bering Sea region. Thus, any differences in the regional composite structures might provide additional insight into the relative importance of surface processes in forcing rapid cyclolysis. We are currently undertaking a more detailed investigation of these regional differences and intend to compare them to similarly constructed composites of RCP cyclones in the North Atlantic, where orographic influences are presumably even weaker than in the Bering Sea region.

The composite negatively tilted, 500-hPa trough (which becomes progressively more negatively tilted with time) exhibits an upper-level evolution reminiscent of the so-called LC2 life cycle presented by Thorncroft et al. (1993, hereafter THM) in their examination of the influence of barotropic shear on the structure and evolution of baroclinic waves. They showed that cyclonic, meridional, barotropic shear in the zonal mean flow produced storms characterized by negatively tilted, cut-off upper-level PV waves. A large fraction of the TFP–RCP cyclones observed in the North Pacific Ocean in our 11-yr sample occurred during the warm phase of ENSO (El Niño). Recent work by M. A. Shapiro et al. (1999, personal communication) examined the effects of ENSO on extratropical life cycles in the North Pacific Ocean. They suggested that the different phases of ENSO impose different time mean meridional shears on the North Pacific wintertime atmospheric circulation by modulating the intensity and position of the seasonal time mean jet stream over the northeastern Pacific. They found that El Niño (La Niña) favors cyclonic, LC2-type (anticyclonic, LC1 type) breaking of upper-level PV waves in the region. Thus, our sample, which was taken over a period during which La Niña was rare, is consistent with their suggestion in that the composite reflects a bias toward LC2-like structures.

In terms of the actual cyclolysis, however, the observations presented here conflict with theoretical expectations based upon the idealized experiments of THM. In those experiments, the LC1 life cycle exhibited a much more rapid decrease in eddy kinetic energy than did the LC2 life cycle (see their Fig. 4). This result implies that rapid decay should be more likely in LC1-type storms. Our composite results, however, suggest that something different may be occurring in nature, at least in the North Pacific Ocean, where the composite 500-hPa evolution more closely resembles the LC2 life cycle, at least until the onset of rapid decay. Although some of this difference may arise from the artificial exclusion of diabatic and frictional processes in the idealized model, additional observational and theoretical research must be undertaken before moderate and rapid cyclolysis can be understood in the context of such life cycle experiments.

Given that the mean flow within which a cyclone develops affects its structural evolution, it is also likely that the mean flow affects aspects of its decay. Subsequent work will examine the heat and momentum fluxes associated with rapidly decaying cyclones in the North Pacific in order to determine the role these storms play in maintaining or altering the large-scale flow within which they progress through their life cycles. Finally, in order to more fully understand the nature of a single cyclolysis event, a detailed examination of the physical processes that conspire to produce an RCP is a necessary complement to the current work. Such an analysis is offered in Part II, where a case study of a particularly robust example of North Pacific cyclolysis is examined.

Acknowledgments. We would like to thank Drs. Michael Morgan and Gregory Postel for helpful comments during the course of this work. The thorough and constructive comments of Dr. John Nielsen-Gammon and an anonymous reviewer are also appreciated. This research was supported by the National Science Foundation under Grant ATM-9733127.

REFERENCES

Baker, W. E., 1983: Objective analysis and assimilation of observational data from FGGE. *Mon. Wea. Rev.*, **111,** 328–342.

Bell, G. D., and L. F. Bosart, 1989: A 15-year climatology of Northern Hemisphere 500 mb closed cyclone and anticyclone centers. *Mon. Wea. Rev.,* **117,** 2142–2163.

Bjerknes, J., and H. Solberg, 1922: Life cycle of cyclones and the polar front theory of atmospheric circulation. *Geofys. Publ.,* **3,** 1–18.

Blackmon, M. L., J. M. Wallace, N. C. Lau, and S. L. Mullen, 1977: An observational study of the Northern Hemisphere wintertime circulation. *J. Atmos. Sci.,* **34,** 1040–1053.

Chang, E. K. M., 2000: Wave packets and life cycles of troughs in the upper troposphere: Examples from the Southern Hemisphere summer season of 1984/85. *Mon. Wea. Rev.,* **128,** 25–50.

Gyakum, J. R., J. R. Anderson, R. H. Grumm, and E. L. Gruner, 1989: North Pacific cold-season surface cyclone activity: 1975–1983. *Mon. Wea. Rev.,* **117,** 1141–1155.

Hobbs, P. V., J. D. Locatelli, and J. E. Martin, 1996: A new conceptual model for cyclones generated in the lee of the Rocky Mountains. *Bull. Amer. Meteor. Soc.,* **77,** 1169–1178.

Horel, J. D., and J. M. Wallace, 1981: Planetary scale atmospheric phenomena associated with the interannual variability of sea-surface temperature in the equatorial Pacific. *Mon. Wea. Rev.,* **109,** 813–829.

Hoskins, B. J., I. Draghici, and H. C. Davies, 1978: A new look at the ω-equation. *Quart. J. Roy. Meteor. Soc.,* **104,** 31–38.

——, M. E. McIntyre, and A. W. Robertson, 1985: On the use and significance of isentropic potential vorticity maps. *Quart. J. Roy. Meteor. Soc.,* **111,** 877–946.

Kidson, J. W., and M. R. Sinclair, 1995: The influence of persistent anomalies on Southern Hemisphere storm tracks. *J. Climate,* **8,** 1938–1950.

Kreitzberg, C. W., 1968: The mesoscale wind field in an occlusion. *J. Appl. Meteor.,* **8,** 53–67.

Lefevre, R. J., and J. W. Nielsen-Gammon, 1995: An objective climatology of mobile troughs in the northern hemisphere. *Tellus,* **47A,** 638–655.

Le Truet, H. L., and E. Kalnay, 1990: Comparison of observed and simulated cyclone frequency distribution as determined by an objective method. *Atmosfera,* **3,** 57–71.

Martin, J. E., 1998: The structure and evolution of a continental winter cyclone. Part I: Frontal structure and the occlusion process. *Mon. Wea. Rev.,* **126,** 303–328.

——, 1999: Quasigeostrophic forcing of ascent in the occluded sector of cyclones and the trowal airstream. *Mon. Wea. Rev.,* **127,** 70–88.

Palmen, E., 1951: The aerology of extratropical disturbances. *Compendium of Meteorology,* T. F. Malone, Ed., Amer. Meteor. Soc., 599–620.

Penner, C. M., 1955: A three-front model for synoptic analysis. *Quart. J. Roy. Meteor. Soc.,* **81,** 89–91.

Reed, R. J., 1979: Cyclogenesis in polar air streams. *Mon. Wea. Rev.,* **107,** 38–52.

Roebber, P. J., 1984: Statistical analysis and updated climatology of explosive cyclones. *Mon. Wea. Rev.,* **112,** 1577–1589.

Sanders, F., 1988: Life history of mobile troughs in the upper westerlies. *Mon. Wea. Rev.,* **116,** 2629–2648.

——, and J. R. Gyakum, 1980: Synoptic-dynamic climatology of the ''bomb.'' *Mon. Wea. Rev.,* **108,** 1589–1606.

Schultz, M. A., and C. F. Mass, 1993: The occlusion process in a midlatitude cyclone over land. *Mon. Wea. Rev.,* **121,** 918–940.

Shapiro, M. A., and D. Keyser, 1990: Fronts, jet streams, and the tropopause. *Extratropical Cyclones, The Erik Palmén Memorial Volume,* C. W. Newton and E. O. Holopainen, Eds., Amer. Meteor. Soc., 167–191.

Sinclair, M. R., 1994: An objective cyclone climatology for the Southern Hemisphere. *Mon. Wea. Rev.,* **122,** 2239–2256.

——, 1995: A climatology of cyclogenesis for the Southern Hemisphere. *Mon. Wea. Rev.,* **123,** 1601–1619.

——, 1996: A climatology of anticyclones and blocking for the Southern Hemisphere. *Mon. Wea. Rev.,* **124,** 245–263.

——, 1997: Objective identification of cyclones and their circulation intensity, and climatology. *Wea. Forecasting,* **12,** 595–612.

Thorncroft, C. D., B. J. Hoskins, and M. E. McIntyre, 1993: Two paradigms of baroclinic-wave life-cycle behaviour. *Quart. J. Roy. Meteor. Soc.,* **119,** 17–55.

Wallace, J. M., and D. S. Gutzler, 1981: Teleconnections in the geopotential height field during the Northern Hemisphere winter. *Mon. Wea. Rev.,* **109,** 784–812.

——, G.-H. Lim, and M. L. Blackmon, 1988: Relationship between cyclone tracks, anticyclone tracks and baroclinic waveguides. *J. Atmos. Sci.,* **45,** 439–462.

Wolter, K., and M. S. Timlin, 1993: Monitoring ENSO in COADS with a seasonally adjusted principal component index. *Proc. 17th Climate Diagnostics Workshop,* Norman, OK, NOAA/NMC, 52–57.

Zishka, K. M., and P. J. Smith 1980: The climatology of cyclones and anticyclones over North America and surrounding ocean environs for January and July, 1950–1977. *Mon. Wea. Rev.,* **108,** 387–401.